There may be differences between this version and the published version. You are advised to consult the published version if you wish to cite from it.

[http://eprints.gla.ac.uk/266613/](http://eprints.gla.ac.uk/266613/)

Deposited on 24 May 2022

**1** **Influence of different additives on the rheology and microstructural development of MgO-**

**2** **SiO$_2$ mixes**

**3**

**4** Sanjeev Kumar[a,b], Jiawei Lei[b], En-Hua Yang[b], Cise Unluer[c,*]

**5**

**6** [a] Engineering Systems and Environment, University of Virginia, Thornton Hall,

**7** Charlottesville, VA 22904, United States

**8** [b] School of Civil and Environmental Engineering, Nanyang Technological University, 50

**9** Nanyang Avenue, Singapore 639798, Singapore

**10** [c] School of Engineering, University of Glasgow, G12 8LT, Glasgow, United Kingdom

**11** *\* Corresponding author. E-mail address: Cise.Unluer@glasgow.ac.uk*

**12**

**13** **Abstract:** Development of alternative binder systems to be used in additive and automated

**14** manufacturing technologies is crucial for increasing the sustainability and productivity of the

**15** construction process. Advancements in this area facilitate shorter construction durations,

**16** enhanced resource efficiency and reduced construction waste; enabling complex, high-

**17** quality and functional designs that would not be possible with traditional methods. The

**18** novelty of this work involves the demonstration of the properties of a promising alternative

**19** binder, reactive MgO-SiO$_2$ (RMS) binder, that can highlight its feasibility to be used in large-

**20** scale applications and the identification of the effects of different phosphate additives during

**21** this process. RMS mixes containing three different phosphate additives (sodium

**22** hexametaphosphate, trimetaphosphate and orthophosphate (OP)) were analyzed for their

**23** pH, reaction kinetics, workability, mechanical performance and rheological properties to

**24** reveal the influence of these additives on the properties of RMS mixes. These findings were

**25** supported by FTIR, $^{29}$Si MAS NMR and XRD measurements. The inclusion of OP in RMS binder

**26** systems increased the pH of solution, thereby improving the dissolution of silica and its

**27** reaction with Mg-phases and resulting in enhanced magnesium-silicate-hydrate (M-S-H)

**28** formation. These improvements in hydration mechanisms translated into better mechanical

**29** performance and rheological properties, which can correlate to desirable properties for 3D

**30** printing applications.

**31**

**32** **Keywords:** Reactive magnesia cement; M-S-H; rheology; viscoelasticity; 3D printing

33

## 1. Introduction

35

Considering the high $CO_2$ emissions and energy use associated with the construction industry, there is a need to identify alternative building materials with lower environmental impacts. One potential alternative being considered is reactive magnesium oxide (MgO) cement (RMC), which requires lower calcination temperatures when compared to traditional Portland cement (PC) and can be obtained from waste resources such as reject brine [1-3]. The two main routes of strength development within RMC formulations have been defined as (i) the carbonation of RMC to form a range of hydrated magnesium carbonate (HMC) phases [4, 5] and (ii) its reaction with a silica source to form magnesium silicate hydrate (M-S-H) [3, 6-8]. The hydration of periclase (MgO) in the presence of added silica ($SiO_2$) leads to the formation of a colloidal gel like structure, indicating the presence of M-S-H [9, 10]. Due to its ability to provide binding strength within a relatively low pH environment, M-S-H based binders have been considered for nuclear-waste-encapsulations or contaminant immobilization applications [11, 12].

49

The formation of M-S-H gel involves several reactions that initiate with the dissolution of MgO, precipitation of brucite and the reaction of Mg-phases with the hydrated silica to form M-S-H [11]. The extent and degree of M-S-H formation depends on the availability of $Mg^{2+}$ and $OH^-$ to react with the dissolved silica, influenced by factors such as the initial pH of the solution. Recent studies [1, 8, 13, 14] have indicated that the precipitation of M-S-H can be significantly affected by the use of phosphate admixtures such as sodium hexametaphosphate ($Na_6O_{18}P_6$, HMP). This precipitation influences the retardation/acceleration of setting times and hardening of reactive $MgO-SiO_2$ (RMS), which can serve as an alternative binder with cementing properties. Accordingly, controlling the reaction rates can enable the achievement of the desired workability and performance without increasing the water/binder (w/b) ratio.

60

While various admixtures are used to enhance the properties of PC-based mixes [15-18] the main superplasticizer that has been used in RMS-based mixes so far is HMP, which was shown to improve the fresh properties of the resulting mixes [6, 19, 20]. The inclusion of a small amount of HMP in RMS systems was shown to inhibit the formation of brucite during the

65    hydrolysis of MgO, without suppressing the formation of M-S-H [20]. While this modification

66    can significantly alter the fresh properties of RMS mixes by inducing different reaction

67    pathways, the effect of different phosphate additives on the fresh and hardened properties

68    of RMS systems has not been studied in detail until now. One potential application, in which

69    these additives would play a key role is 3D printed concrete. Previous studies explored the

70    use of faster vertical building rates by predicting the print speed and vertical filament height

71    in 3D printing [21]. Production of different building components via the use of 3D printing

72    could not only contribute to construction productivity but also increase the quality of the final

73    products, meanwhile offering higher geometrical freedom, efficient use of natural resources,

74    and higher cost-efficiency and universality [22].

75

76    One of the main factors to consider during the development of a printable cementitious mix

77    is the optimization of its thixotropic properties so that the final mix can be easily extruded

78    during the printing process, while it maintains its original shape and bears the load of the

79    subsequent layers without any deformation after deposition. The shape retention capacity is

80    not only a prerequisite for surface aesthetics of the printed layers but also a requirement for

81    structural buildability [23]. Accordingly, several factors such as the mix design and chemical

82    and physical interaction amongst the mix components influence this property. One factor to

83    consider is the flocculation effect of the powder particles within the prepared formulations.

84    The links between the particles can be broken under shearing, which can then be re-

85    established once the material is at rest [24, 25]. In this respect, the properties of the binder

86    and any additives (e.g. admixtures) used as a part of the mix design and their effect on the

87    flowability of the resulting concrete formulations play a major role in the 3D printing process

88    [26, 27].

89

90    The binders that are preferred for 3D printing applications are semi-stiff at rest but start to

91    flow when agitated [28]. Further research also focused on the use of supplementary

92    cementitious materials (SCMs) [29] and fiber reinforcement [30, 31] to impart the required

93    yield strength and mechanical performance of 3D printed concrete composites. While

94    previous studies [32] looked into the potential use of RMC in 3D printing via the inclusion of

95    various additives to maintain a sufficient flowability during printing and the adjustment of the

96    extrusion pressure, the feasibility of RMS systems to be used in 3D printing applications has

not been investigated until now. When compared to PC, RMS systems possess similar hydration mechanisms and kinetics, which could present an advantage by enabling the printing of complex structures that could gain strength without the need for any special curing conditions, as those usually required by RMC systems. While the pH of RMS systems is generally lower than PC systems, alternative reinforcements (e.g. natural and synthetic fibers) could be successfully integrated into the mix design. In this respect, previous and ongoing studies [33]-[34, 35] have demonstrated the incorporation of non-metallic (e.g. polyvinyl alcohol (PVA)) and cellulosic fibers as a feasible option to widen possible application areas of RMC and RMS systems.

The novelty of the work presented in this paper involves the demonstration of the effect of different additives on the reaction kinetics that led to improved rheological parameters and mechanical performance, desirable properties for 3D printing applications. Differing from the existing studies on RMS mixes, the role of various phosphate additives such as sodium hexametaphosphate ($Na_6O_{18}P_6$, HMP), sodium trimetaphosphate ($Na_3O_9P_3$, TMP) and sodium orthophosphate ($Na_3O_4P$, OP) on the factors influencing the rheology (e.g. structural evolution and viscoelasticity) of RMS systems was highlighted. This was achieved via the measurement of flow, pH, heat of hydration, strength, which was further supported by a detailed microstructural assessment to identify the changes in phase formations within the prepared mixes.

## 2. Materials and Methodology

### 2.1 Materials and sample preparation

RMC was supplied by Richard Baker Harrison (UK), whereas Microsilica (MS) was provided by Elkem (Singapore). Table 1 shows the chemical compositions of these materials. Their particle size distributions (PSD), displayed in Fig. 1, were obtained via a Malvern Mastersizer 2000. Out of the superplasticizers used in the prepared mixes, HMP was supplied by VWR International (Singapore); whereas OP and TMP were supplied by Sigma Aldrich (Singapore).

129    Three types of RMS mixes were prepared, containing equal parts (50/50) of RMC and MS by

130    mass. The w/b ratio of all mixes was kept constant at 0.4. All the phosphate additives (HMP,

131    OP and TMP) were included at a fixed ratio of 1% by mass of binder to enable their direct

132    comparison. The mixtures were prepared according to ASTM C 305 specifications. All the

133    additives were pre-mixed for about 60 s before their introduction into the binder [36]. Mixing

134    was continued until a thorough workable paste was obtained, which was then cast into

135    50×50×50 mm cubic specimens and cured under sealed conditions (30±1°C, RH 95±1%) for 28

136    days.

137



138
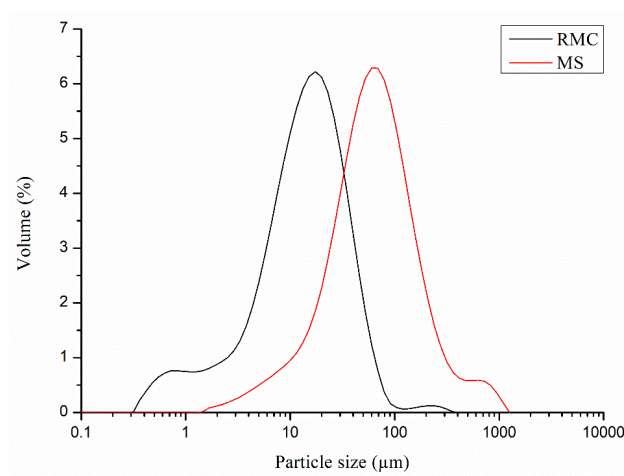
139    **Fig. 1** Particle size distribution of RMC and MS

140

141

142    **2.2 Methodology**

143

144    **2.2.1   Measurement of pH, flow, calorimetry and compressive strength**

145

146    The pH measurements of the respective samples after 3, 7 and 28 days of curing were

147    performed by a Mettler Toledo pH meter, with an accuracy of ±0.01. The sample fractions

148    were mixed, after which they settled in distilled water at a ratio of 1:10, before testing. All pH

149    measurements were conducted in triplicates and the average values were recorded.

150

151    The flow test was carried out immediately after mixing, according to ASTM C1437-07 [37]. As

152    a part of the initial step, each paste was placed in a conical brass mold, with a uniform tamping

153 of 20 times/layer. Once each paste was placed in the mold uniformly, the mold was removed

154 to start the manually controlled flow table test. The pastes are allowed to vibrate as the table

155 dropped from a height of 12.5 mm. The dropping procedure was repeated 25 times within 15

156 s and the average flow was calculated as a result of four diameter measurements taken at

157 equally spaced intervals.

158

159 The heat generated during the hydration of the prepared samples was monitored for the first

160 3 days with an I-Cal 8000 calorimeter, in line with ASTM C1702-15A [38]. The internal

161 temperature was stabilized at 26°C before placing the samples in the calorimeter. The

162 preparation and placement of samples inside the chamber were done as quickly as possible

163 to avoid any delays in measurement.

164

165 The compressive strength data were generated by testing samples in triplicates obtained by

166 using a uniaxial Toni Technik frame, at a loading rate of 55 kN/min, according to ASTM

167 C109/C109M-16A [39].

168

169

170 **2.2.2    Microstructural characterisation**

171

172 Fragments collected from each sample after 24 h and 3 d of curing were studied further via

173 attenuated total reflectance-Fourier transform infrared spectroscopy (ATR-FTIR), magic angle

174 spinning nuclear magnetic resonance (MAS NMR) and x-ray diffraction (XRD) analyses. For all

175 microstructural observations, samples were stored in a solvent exchange solution (i.e.

176 isopropanol) for 3 d to accurately analyze the extent of hydration at a given point. The

177 powders were ground to achieve a particle size of < 75 μm before further analysis.

178

179 ATR-FTIR, at a scan range between 650 and 4000 cm$^{-1}$, was completed via a spectrometer

180 manufactured by Perkin Elmer, at a resolution of 4 cm$^{-1}$. The attenuated wave was measured

181 by establishing a good contact between the instrument surface and the powdered specimen.

182

183 $^{29}$Si MAS NMR experiments were performed on a Bruker Advance III HD 600 spectrometer

184 (14.1 T) using a 4 mm zirconia rotor, with a spinning speed of 10 kHz. Spectra were acquired

6

185  at 119.24 MHz with a 90° pulse of 4 µs, recycle delay of 60 s and 700 scans. The chemical shifts

186  were externally referenced to tetraethoxysilane (TEOS) at -82.04 ppm. The deconvolutions of

187  the spectra were conducted using the minimum numbers of component peaks to describe

188  the spectra. The spectra were fitted by using Gaussian-Lorentzian Sum function with mainly

189  Gaussian for $Q^3$ and $Q^4$ peaks and mainly Lorentzian for $Q^1$ and $Q^2$ peaks as described in [10,

190  40], where Q referred to tetrahedrally coordinated silicon and the superscripts represented

191  the number of siloxane bridges. Constant peak shapes and widths for each identified species

192  were maintained throughout the deconvolution process.

193

194  The XRD data, obtained by a D8 Advance Bruker device, were collected for samples cured for

195  1 and 3 d. The analysis took place at 0.02° 2θ per step, within a range of 10°-70° 2θ. The

196  quantification of crystalline hydration products was performed via an external standard

197  method as suggested in Scrivener, Snellings and Lothenbach [41]. The amorphous content

198  was determined through an iterative Rietveld-PONCKS [42] with TOPAS software (Bruker,

199  release 5.0).

200

201

202  **2.2.3   Structural evolution and viscoelasticity**

203

204  The structural evolution of RMS mixes was characterized using the storage modulus and

205  phase angle. A Thermo Haake Mars-III rheometer with rotational parallel plates was used to

206  carry out the rheological measurements. The adopted disc diameter was 20 mm and the gap

207  between the plates was maintained at 1 mm. To eradicate possible gap positioning shifts, the

208  poured samples were pre-sheared at a rotational speed of 100/s for 30 s. Throughout the test,

209  the temperature of the testing setup was maintained at 20±0.5°C. Strain sweep test was

210  conducted at a strain amplitude ranging from 0.001% to 10%, with a constant frequency of 2

211  Hz to determine the changes in the linear viscoelastic region. The rheological parameters

212  adopted during this testing were similar to those used in previous studies for the assessment

213  of the structural recovery of cementitious systems [43-45]. Upon the completion of

214  rheological measurements, the pastes between the plates were closely monitored to ensure

215  there were no signs of bleeding or excessive agglomeration.

216

217

## 3. Results and Discussion

219

### 3.1 pH

221

Fig. 2 indicates the pH values of pure RMS as well as RMS samples containing HMP, OP and TMP. The pH of aqueous solutions containing these individual phosphate additives were recorded as 8.36, 8.75 and 12.14 for TMP, HMP and OP, respectively. The initial (i.e. at 0 d) pH values for RMS, RMS-TMP, RMS-HMP and RMS-OP samples were measured as 10.9, 11.3, 11.6 and 11.9, respectively. Measured at 72 h, a decline in the pH was observed, resulting in a much lower pH for RMS (9.3) when compared to those of RMS-TMP (10.1), RMS-HMP (10.3) and RMS-OP (11.1) samples.

229

The higher pH at initial stages was associated with the dissolution of silica, which further reacted with $Mg^{2+}$ ions to form M-S-H [46]. A gradual decrease in the pH of all samples was observed over time, although this decline was much faster during the first 7 days, indicating that a majority of the dissolution and precipitation took place during this period. The initial decline in pH was associated with the precipitation of brucite, followed by its reaction with silica to form M-S-H [2, 13].

236

The differences in the pH values of RMS mixes containing different phosphate additives in comparison to the control mix (RMS) were linked with the adsorption of $PO_4^{3-}$ on the MgO surface [20, 46]. The higher pH values revealed by the RMS-OP mix when compared to RMS-HMP, RMS-TMP and RMS mixes at all durations could be an indication of the increased silica dissolution and its subsequent reaction with Mg-phases, possibly resulting in the enhanced precipitation of M-S-H in RMS-OP mixes.

243

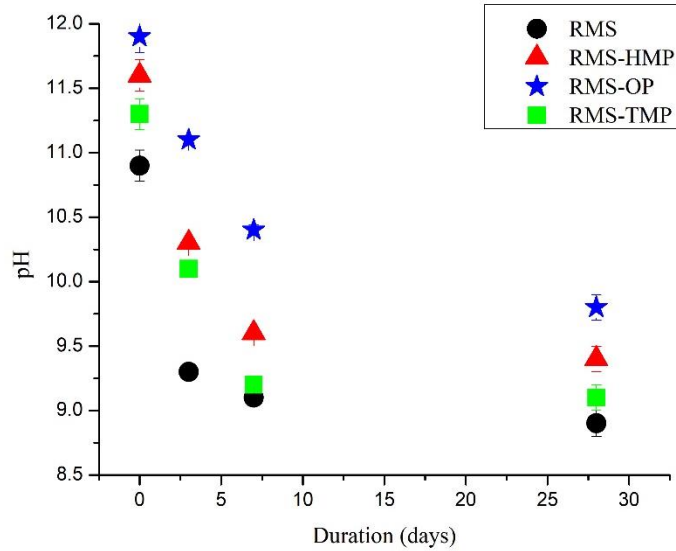**Fig. 2** pH of all samples measured over a period of 28 d

## 3.2 Workability

The influence of each of the different phosphate additives on the fluidity of RMS formulations was investigated via the use of the flow table test, as shown in Fig. 3. Amongst the three phosphate additives used in this study, RMS-TMP revealed the highest flow of 12.3 cm, followed by RMS-HMP at 11.8 cm. On the other hand, RMS-OP showed a 11.5 cm flow, which was comparable with the flow demonstrated by the control mix, RMS (11.2 cm). The variations in the flow values amongst these samples could be associated with the different adsorption rates of $PO_4^{3-}$ on the surfaces of MgO particles demonstrated by OP, HMP and TMP additives, which delayed the formation of Mg-based hydrate phases within RMS systems [47]. In line with the results obtained here, earlier studies on concrete 3D printing involving the use of limestone filler indicated a loss in workability [48], similar to the trend observed in RMS-HMP and RMS-TMP mixes. Alternatively, RMS-OP mixes demonstrated a consistent workability over time, which could present an advantage in 3D printing applications.

9

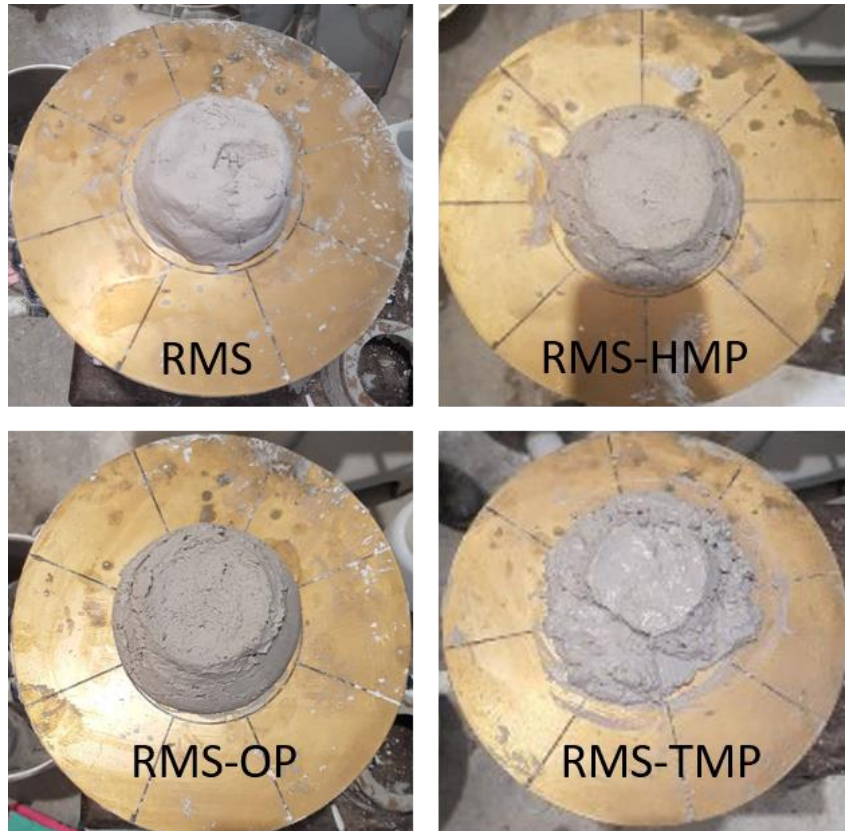**Fig. 3** Workability of all samples

### 3.3 Heat of hydration

Fig. 4(a) indicates the heat flow revealed by all mixes during the first 72 h of hydration. Unlike PC-based mixes, RMS mixes did not reveal a single hydration peak but rather a gradual increase in heat flow, resulting in wide curves, which could differ in line with the phosphate additive used, as could be seen during the first 72 h. A similar outcome was revealed by previous studies that looked into the hydration mechanisms of RMS mixes [6, 7]. When compared to the control mix (RMS), RMS-OP and RMS-HMP mixes demonstrated a significant amount of early dissolution, resulting in a higher amount of heat release during the initial stages. Amongst all mixes, RMS-OP, which also revealed the highest pH values at all times (Fig. 2), achieved the largest heat flow. On the other hand, RMS mix revealed the least amount of heat, which was an indication of the limited dissolution and precipitation processes, in line with the findings of previous studies [7]. Although RMS-TMP mix demonstrated an increase

10

280   in its heat flow after ~30 h of hydration, the initial stage of reaction was dominated by a

281   dormant period of limited heat flow.

282

283   Fig. 4(b) shows the cumulative heat evolved in each mix during the 72 h of hydration.

284   Following the trend observed in the heat flow measurements, the control mix (RMS) indicated

285   the lowest exothermic output, which was an indication of its limited hydration in comparison

286   to other mixes. Although its reaction rate started increasing after the first ~30 h, RMS-TMP

287   mix revealed a similar heat release with the control mix, which was in line with their

288   comparable pH values reported earlier. Differing from these two mixes, RMS-OP and RMS-

289   HMP achieved higher heat releases throughout the first 72 h of hydration, which could be an

290   indication of the increased precipitation of hydrate phases such as M-S-H through the

291   improved dissolution and reactivity of silica occurring in these mixes. Amongst all samples,

292   the highest cumulative heat was revealed by the RMS-OP mix, which corresponded with the

293   highest pH values demonstrated by this mix, enabling the enhancement of the hydration

294   reaction. These findings were in line with those reported by earlier studies [46], where the

295   increased precipitation of Mg-based hydrate phases in the presence of OP, as opposed to
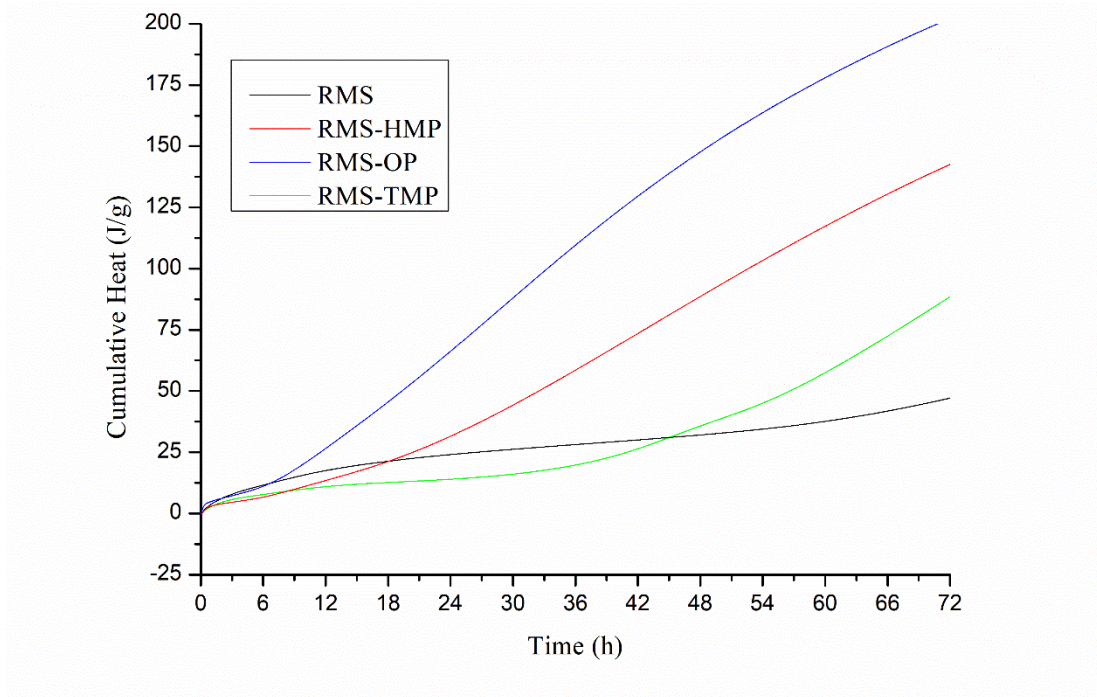
296   HMP and TMP, was observed.

297



298

299                                        (a)

11
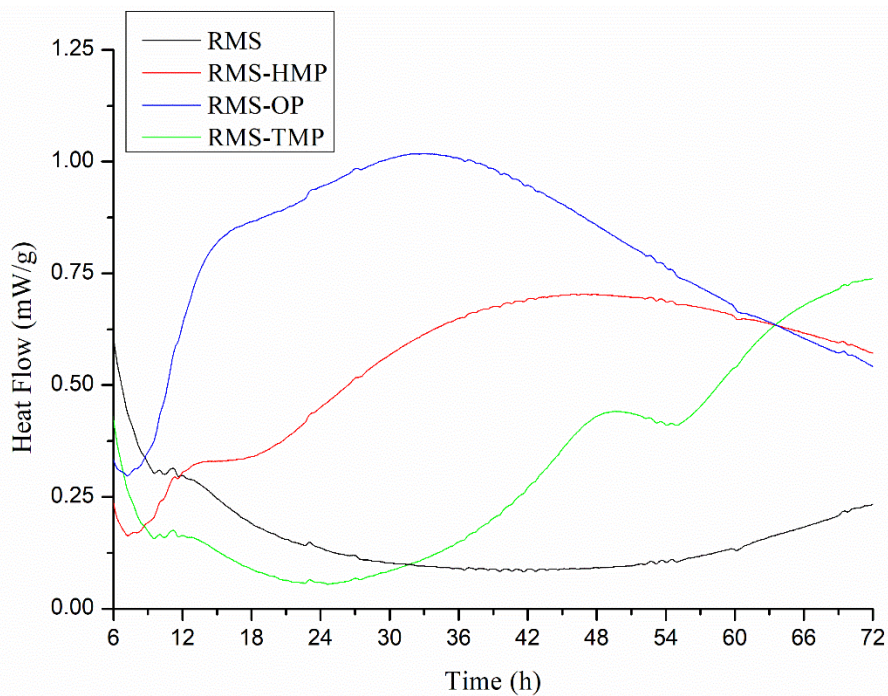
(b)

**Fig. 4** Isothermal calorimetry results for all samples during the first 72 h, showing the (a) heat flow and (b) cumulative heat curves

## 3.4 Compressive strength

The strength development of all mixes over a period of 28 d is shown in Fig. 5. A steady increase in strength displayed by all samples indicated the hydration progress during the assessment period. This improvement in the performance of RMS samples was associated with the formation of hydrate phases such as M-S-H, which contributed to the establishment of a dense and stable microstructure [3, 6, 7].
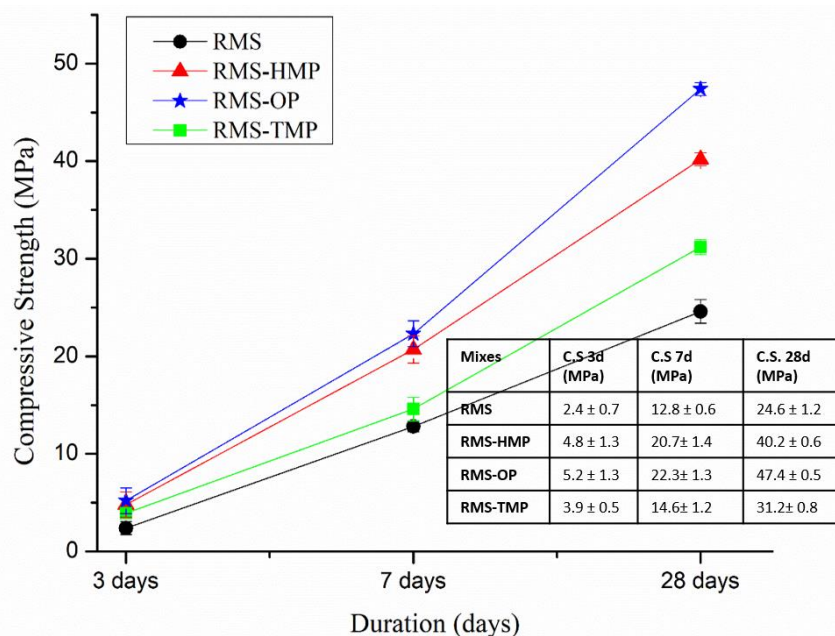
Starting with early ages, RMS-OP mix achieved the highest strengths amongst all samples, followed by RMS-HMP and RMS-TMP mixes. All mixes involving the use of phosphate additives demonstrated consistently higher strengths than the control mix (RMS) at all times. At early stages (3 d), the differences in strength were not as pronounced, during which most mixes revealed similar strengths. Accordingly, RMS-HMP and RMS-OP mixes revealed comparable strengths at 3 d (4.8 MPa vs. 5.2 MPa) and 7 d (20.7 MPa vs. 22.3 MPa). However,

12

320     the differences in the strength results grew further as the curing duration increased, resulting

321     in a 28-d strength of 47.4 MPa for RMS-OP, which was 48% higher than the corresponding

322     strength of the control mix (24.6 MPa). At the same curing duration (28 d), RMS-HMP and

323     RMS-TMP mixes revealed strengths of 40.2 MPa and 31.2 MPa, respectively.

324

325     The improved performance of the RMS-OP mix was associated with the enhancement of the

326     hydration reaction in the presence of OP, as also confirmed earlier by the pH and isothermal

327     calorimetry results. Earlier studies [49] demonstrated that a high compressive strength, along

328     with rheological properties, were found to be influential in attaining a good dimensional

329     accuracy in concrete 3D printing. Accordingly, early strength development, similar to those

330     observed in RMS-OP and RMS-HMP mixes presented in this study, was also found to be critical

331     in concrete 3D printing applications [50, 51]. When these factors were taken into account, the

332     two best-performing mixes, RMS-OP and RMS-HMP, were chosen for further analysis leading

333     up to their future potential use in 3D printing applications.

334



| Mixes | C.S 3d (MPa) | C.S 7d (MPa) | C.S. 28d (MPa) |
|---|---|---|---|
| RMS | 2.4 ± 0.7 | 12.8 ± 0.6 | 24.6 ± 1.2 |
| RMS-HMP | 4.8 ± 1.3 | 20.7± 1.4 | 40.2 ± 0.6 |
| RMS-OP | 5.2 ± 1.3 | 22.3± 1.3 | 47.4 ± 0.5 |
| RMS-TMP | 3.9 ± 0.5 | 14.6± 1.2 | 31.2± 0.8 |

335

336          **Fig. 5** Compressive strengths of all samples after 3, 7 and 28 d of curing

337

338

339     **3.5 FTIR**

340

341 The FTIR spectra of RMS-HMP and RMS-OP mixes are shown in Fig. 6. The evolution of

342 functional groups in the hydrate phases were studied along the spectral range of 4000-900

343 $cm^{-1}$. All the mixes revealed information on the frequency of $OH^-$ vibrations at 3700-2800 cm$^-$

344 $^1$ [1, 52]. Accordingly, the sharp asymmetrical stretching at 3696 $cm^{-1}$ corresponded to Mg-

345 OH in brucite, whereas $OH^-$ vibrations concerning structural hydroxyl groups in M-S-H were

346 noticed at ~3300 $cm^{-1}$ [7, 9]. When compared to 24 h, these vibrations increased at 3 d,

347 indicating the formation of M-S-H gel. Amongst the two selected mixes, RMS-OP indicated a

348 more extensive dip, which confirmed the increased formation of M-S-H within this mix. The

349 result also paralleled to the earlier observations on M-S-H precipitation, which played a key

350 role in the strength development of RMS formulations.

351

352 The changes in the pH, which were associated with the introduction of different phosphate

353 additives within these mixes, were expected to result in different silica configurations [53, 54].

354 Furthermore, these configurations could alter the viscosity of the mixes through the different

355 extents of gelation occurring between various phases, including the reaction between

356 silicates and the dissolved $Mg^{2+}$ [55]. The silicate interactions could be revealed by

357 investigating the main Si-O-Si band at 1300-800 $cm^{-1}$. Accordingly, Figs. 7 and 8 show the

358 deconvolution of the spectra within this range. These results revealed the differences in the

359 peak width and relevant intensity patterns, which varied with the type of phosphate additive

360 and curing duration.

361

362 Fig. 7 clearly indicates an intensive silica dissolution (990-1050 $cm^{-1}$ and 1100-1200 $cm^{-1}$)

363 occurring in the RMS-OP mix at as early as 24 h. The frequencies 1100-1200 $cm^{-1}$

364 corresponded to the asymmetrical external stretching vibrations ($Q^4$) in Si-O-Si, whereas 990-

365 1050 $cm^{-1}$ reflected the silica vibration ($Q^3$) in M-S-H [10, 56]. At 3 d, the RMS-OP mix revealed

366 an intensive silica bridging within these ranges, reflecting its ability to form M-S-H quicker

367 than its counterpart. Fig. 8 shows the deconvolutions of Si-O-Si within the 800-1300 $cm^{-1}$

368 range, for which the corresponding peak locations are listed in Table 2. The black dotted lines

369 indicate the original FTIR data, whereas the deconvoluted ones are shown in color. At 24 h,

370 the deconvolution patterns of the RMS-HMP mix revealed a small amount of internal and

371 external Si-O-Si stretching vibrations, confirming the dissolution of silica.

372

373    In addition to these vibrations, the RMS-OP mix displayed intensive patterns corresponding

374    to the $Q^3$ silica vibration in M-S-H, thereby indicating the improved precipitation of these

375    hydrate phases [10]. Similarly, the deconvolution patterns revealed by the RMS-OP mix at 3

376    d were more prominent and extensive than RMS-HMP. Accordingly, the higher wave number

377    (1198 cm$^{-1}$) and the extension of existing peaks indicated the formation of larger silicate

378    structures within RMS-OP [54]. In general, the presence of OP is RMS formulations led to

379    peaks with higher intensities and shifts in the peak locations toward higher wavelengths,

380    hinting the increased formation of hydrate phases such as M-S-H . These changes occurring

381    in the Si-O-Si region were accompanied with the structural evolution of M-S-H gel, which

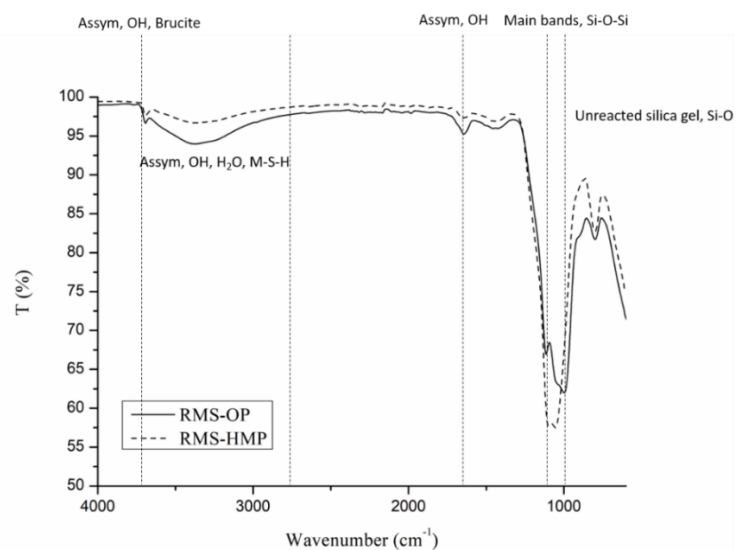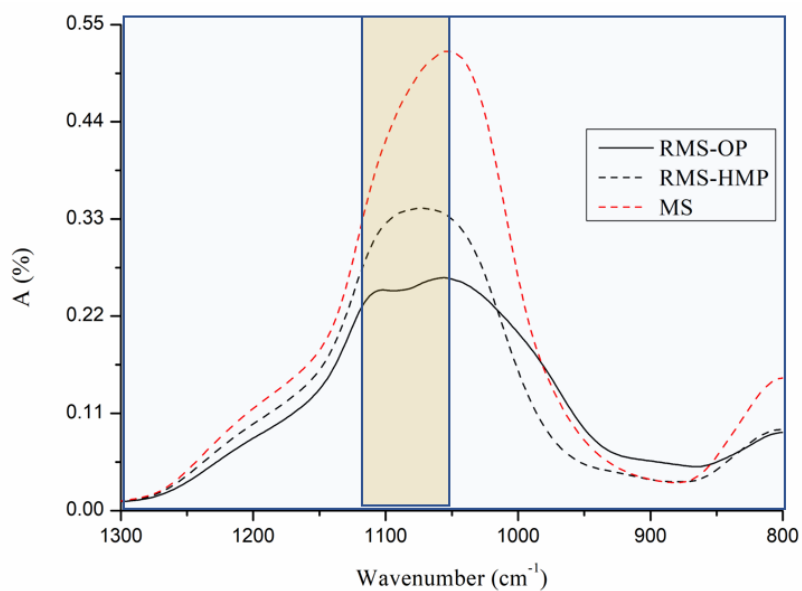382    played a key role in the viscosity of RMS mixes.

383



(a)



386

15

(b)
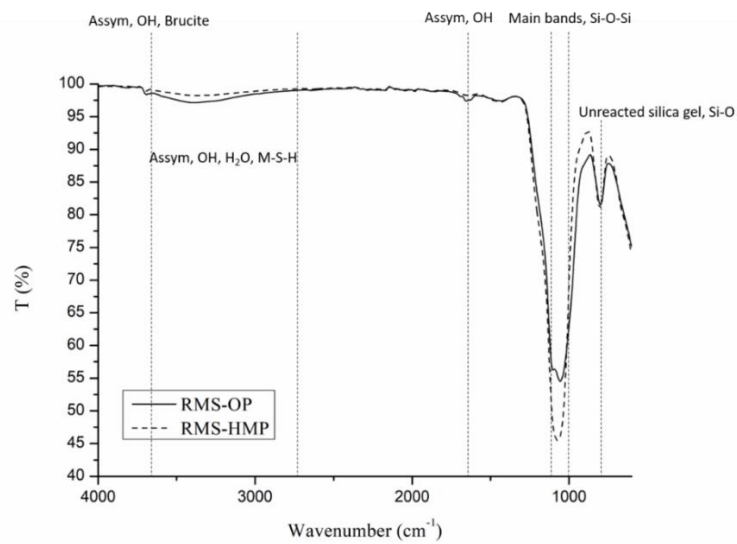
**Fig. 6** FTIR spectra of RMS-HMP and RMS-OP mixes at (a) 24 h and (b) 3 d

(a)
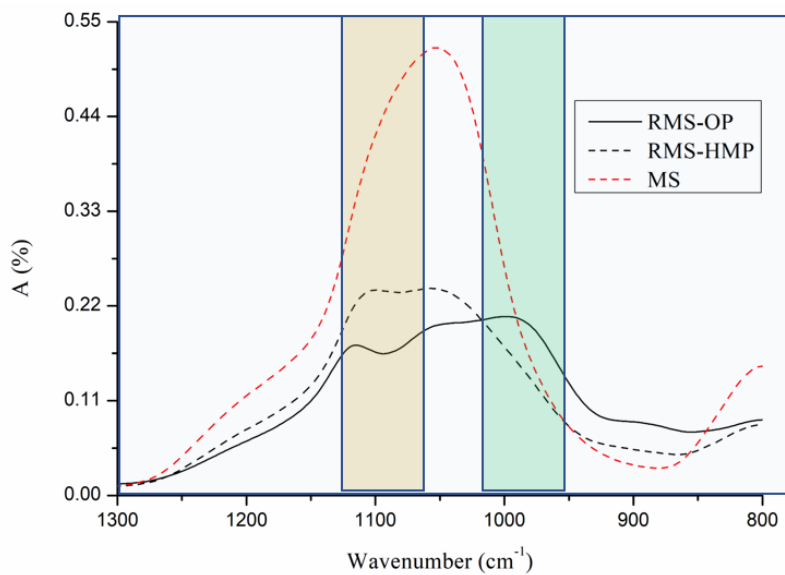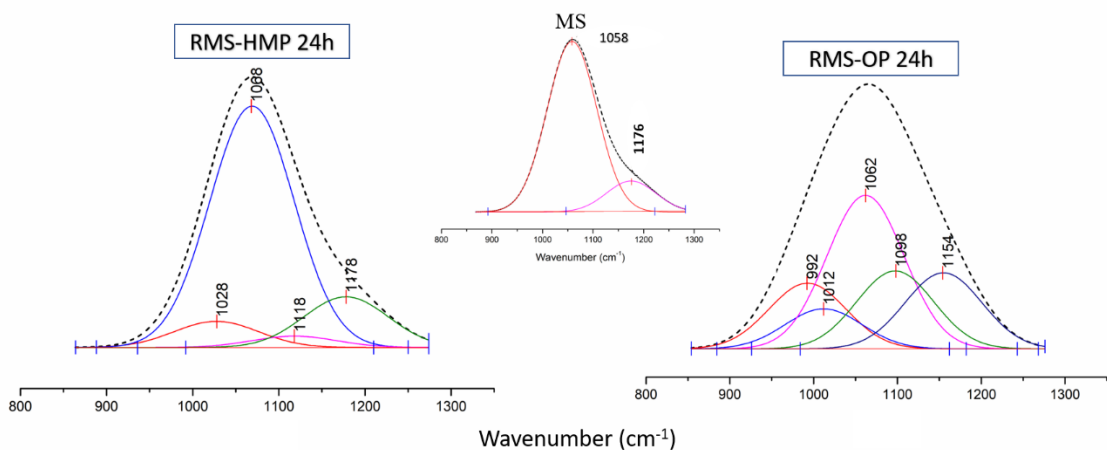
(b)

**Fig. 7** Absorbance spectra of the main bands showing Si-O-Si activity (800-1300 $cm^{-1}$) in

RMS-HMP and RMS-OP mixes at (a) 24 h and (b) 3 d

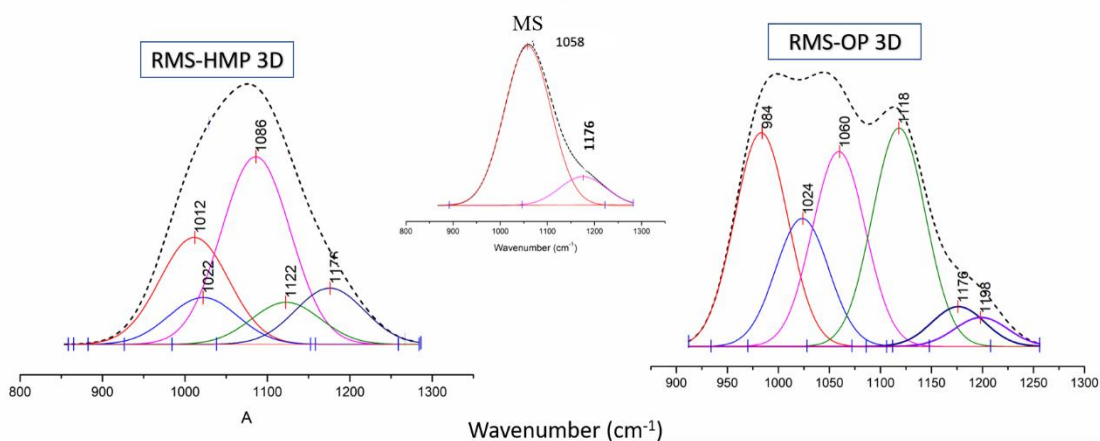**Fig. 8** Deconvolution of the FTIR spectra of the silicate region (800-1300 cm$^{-1}$) in RMS-HMP and RMS-OP mixes at (a) 24 h and (b) 3 d

**3.6 NMR**

The $^{29}$Si MAS NMR spectra of RMS-HMP and RMS-OP mixes are shown in Fig. 9(a). The broadened peak at roughly -111 ppm and the shoulder at -101 ppm represented the fully condensed (($SiO)_4Si$) sites and the hydrated surface sites (($SiO)_3SiOH$) within the unreacted silica fume, respectively [9, 10]. The resonance in the range between -76 and -98 ppm

17

415     indicated the formation of M-S-H, which agreed with the previously reported spectra for

416     synthetic M-S-H [57-59].

417

418     The $^{29}$Si MAS NMR spectra for both mixes were deconvoluted, an example of which (i.e. RMS-

419     OP mix at 3 d) is shown in Fig. 9(b). The chemical shifts and relative intensities of all mixes are

420     summarized in Table. 3. The peak assignments were based on the information available for

421     M-S-H in the literature [57-59] . The results revealed that the spectra primarily consisted of

422     $Q^3$ and $Q^2$ silicate sites, with a small quantity of $Q^1$, indicating the predominant layered silicate

423     structure of M-S-H. The deconvolution of $Q^3$ resonance exhibited two peaks with chemical

424     shifts at roughly -92 ppm and -97 ppm, indicating the two slightly varied Si chemical

425     environments. The major peak $Q^3$(a) at -92 ppm was similar to the $Q^3$ resonance typically

426     identified in antigorite, while the smaller peak $Q^3$(b) at -97 ppm was consistent with the $Q^3$

427     site environment reported for crystalline talc [9, 58].

428

429     The combination of FTIR and NMR results revealed the differences in the silicate

430     connectivities within RMS-OP and RMS-HMP mixes, in which different phosphate additives

431     were used. As seen from both analyses, the spectral details of the RMS-OP mix clearly

432     indicated a different silica configuration. Within this mix, the shift in peak positions to larger

433     ppm might be related with the higher pH values of RMS-OP (Fig. 2), which could have

434     increased the amount of more negatively charged Si-O$^-$ groups that interacted with the

435     positively charged Mg$^{2+}$ ions. This has ultimately led to a higher amount of M-S-H precipitation

436     in the RMS-OP mix when compared to all the other RMS formulations investigated in this
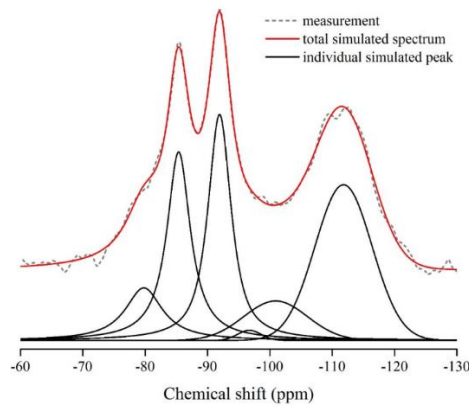
437     study.

438



(a)

18
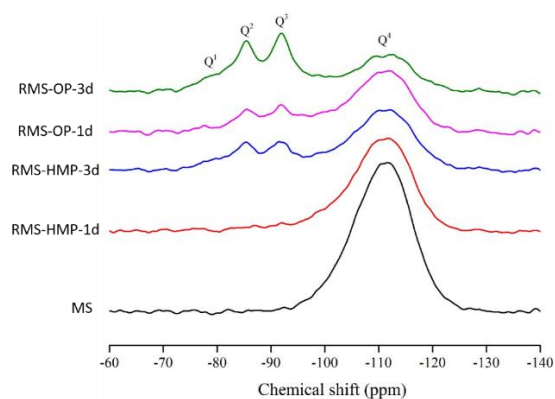
441



442

443 (b)

444 **Fig. 9** (a) ^{29}Si MAS NMR spectra of the RMS-HMP and RMS-OP mixes at 1 d and 3 d, and (b)

445 deconvolution of the [29]Si MAS spectrum (RMS-OP mix at 3 d)

446

447

448 **3.7 XRD**

449

450 The XRD patterns of RMS-HMP and RMS-OP mixes after 1 d and 3 d of curing are shown in Fig.

451 10. Both mixes revealed the presence of unreacted MgO (i.e. main peaks at 42.9° and 62.3°

452 2θ) as well as brucite (i.e. main peak at 38.1° 2θ), indicating the partial conversion of MgO

453 into hydrate phases over time. Both mixes, irrespective of the phosphate additive included in

454 their formulations, indicated the formation of similar phases, which was in line with the

455 findings of previous studies [1-3, 8, 14]. However, the intensities of these phases varied,

456 depending on the reactive capabilities of each phosphate additive used. Even after 1 d of

457 curing, broad amorphous phases of M-S-H at around 33-40° and 58-62° 2θ, which were

458 consistent with those reported in relevant previous literature [6, 7, 46], were observed in both

459 mixes. The higher visibly of these peaks in the RMS-OP mix could explain its better

460 performance [60, 61]. The amorphous hump at 33-40° 2θ for RMS-OP was more notable at 3

461 d, which was accompanied with lower amounts of periclase and brucite than the RMS-HMP

462 mix.

463

464 These observations were confirmed by the quantification of these phases, shown in Table 4.

465 Accordingly, both mixes revealed similar unreacted MgO and brucite contents at 1 d, whereas

RMS-OP contained a higher amount of M-S-H in comparison to RMS-HMP. Increasing the curing duration to 3 d led to a reduction in the unreacted MgO content in both formulations, which was accompanied with an increase in the M-S-H content. Similar to the trend observed at 1 d, RMS-OP revealed a higher M-S-H formation than RMS-HMP, whereas the brucite content in both mixes seemed to reduce over time. These observations were in line with the previous results [46], explaining the reduced formation of brucite formation in the presence of phosphate additives within RMS formulations. The quantification of amorphous phases revealed the decreased presence of amorphous silica (AmS), along with the increased formation of M-S-H in RMS-OP mixes. These phase quantities supported the FTIR and NMR observations, highlighting the increased precipitation of M-S-H over time and within RMS-OP mixes.
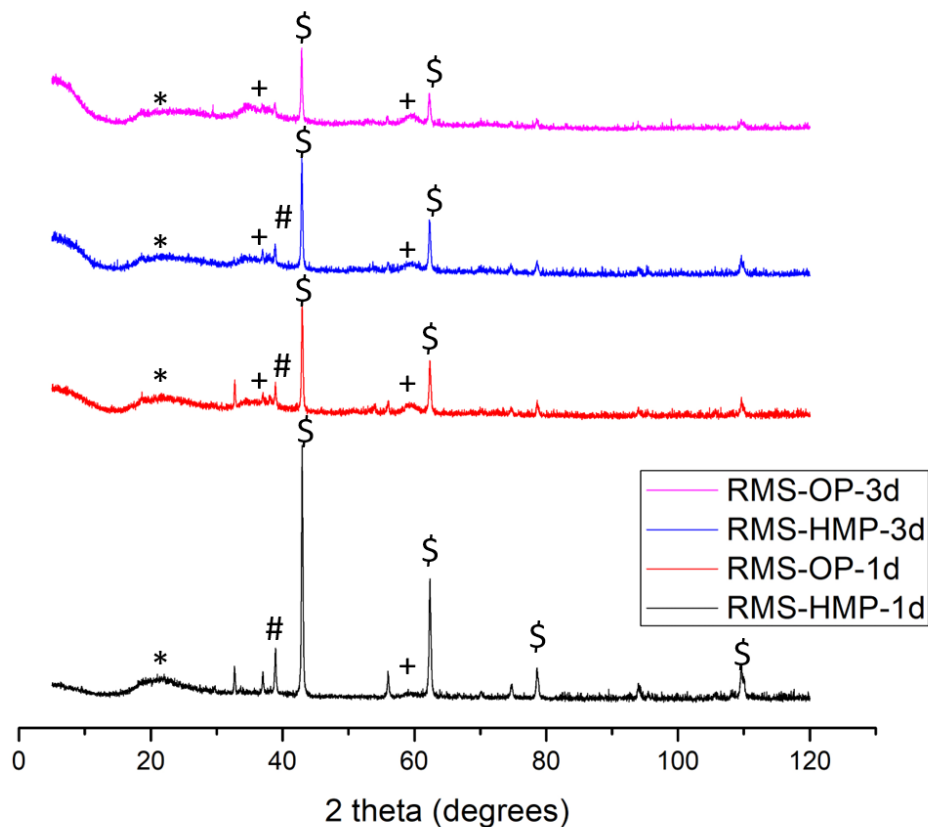


**Fig. 10** XRD patterns of RMS-HMP and RMS-OP mixes

(Symbols: $: Periclase; #: Brucite; *: AmS; +: MSH)

**3.8 Rheology**

Figs. 11 (a) and (b) show the evolution of storage modulus and phase angle of selected RMS mixes, respectively. The storage modulus of all mixes increased, whereas the phase angle measurements decreased when the paste was at rest. These patterns were in line with the findings reported by previous studies on PC-based mixes [24, 55]. In addition to the well-established strong inter-particle interaction forces, others such as Brownian and inertial forces of particles in suspension also need to be considered. These interparticle forces often include steric repulsion, electrostatic or van der Waals forces, which contribute to flocculation when cementitious pastes are at rest [62].

Within the context of RMS mixes, individual cement particles are further held together via the links formed by hydrate phases such as M-S-H, increasing the stiffness and rigidity of the final sample. This action of consolidation in cement suspension often leads to an increased storage modulus and decreased phase angle. All mixes exhibited a steady increase in storage modulus with a steady decrease in phase angle, indicating transitions from viscous to elastic behavior as the analysis approached resting time (900 s). The percolation time (i.e. time when the storage modulus increases steadily or when phase angle stabilizes), was found to be higher in RMS-OP mixes. Accordingly, the addition of OP within RMS mixes drastically increased the storage modulus, resulting in a more elastic behavior when compared to other mixes. The phase angle measurements also reflected the more liquid-like consistencies of RMS and RMS-HMP mixes, which led to a less elastic behavior than the RMS-OP mix.

These observations could be explained by the increased $Mg^{2+}$ and $SiO_3^{2-}$ interactions within the RMS-OP mix, as confirmed earlier by FTIR, NMR and XRD analyses. The higher pH of RMS-OP led to a higher amount of $SiO_3^{2-}$ to react with free $Mg^{2+}$, which further reduced the average distance between cement particles in suspension and increased the van der Waals forces, thereby enhancing the flocculation strength. This mechanism translated into a higher storage modulus and a lower phase angle, highlighting the higher elastic behavior of the RMS-OP mix when compared to other mixes, which could contribute to its ability to be used in 3D printing.

514  Fig. 12 shows the determination of the linear viscoelastic region (LVER) for the selected mixes.

515  The LVER region extended to a critical strain value of 0.002% for the RMS-OP mix, while this

516  value was 0.096% and 0.0005% for RMS and RMS-HMP mixes. Previous studies that involved

517  the analysis of PC mixes by using the same instrumental parameters reported comparable

518  critical strain values of ~0.004% [43, 63]. Furthermore, linear patterns of storage and loss

519  modulus could be easily established with the adopted instrument parameters for the RMS-

520  OP mix in comparison to the RMS-HMP mix. Overall, the rheological measurements revealed

521  that the use of OP in RMS mixes extended the LVER region, enabling a desirable control of

522  paste stiffness and structural integrity that could contribute to their future use in 3D printing

523  applications. Previous studies performed on concrete 3D printing [64] also highlighted the link

524  between the storage modulus of various mixes and properties of printed layers. In this respect,

525  the RMS-OP mix, which demonstrated a trend of increasing storage modulus, could offer

526  enhanced shape retention capability and extrudability when used in additive manufacturing.

527



(a)



(b)

22
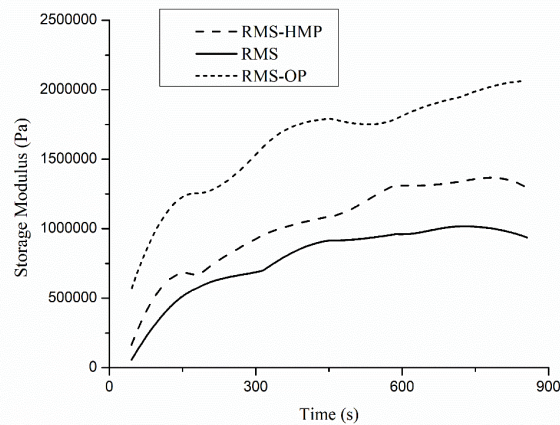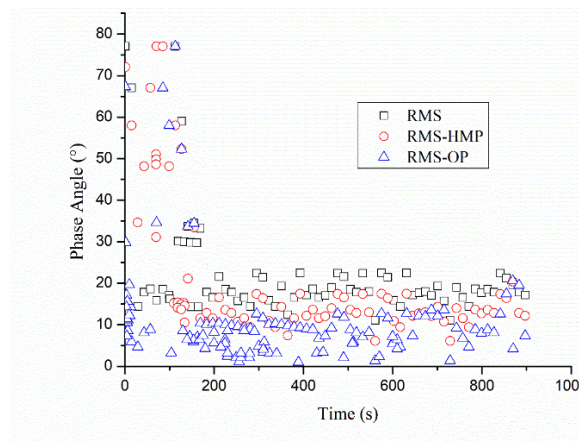
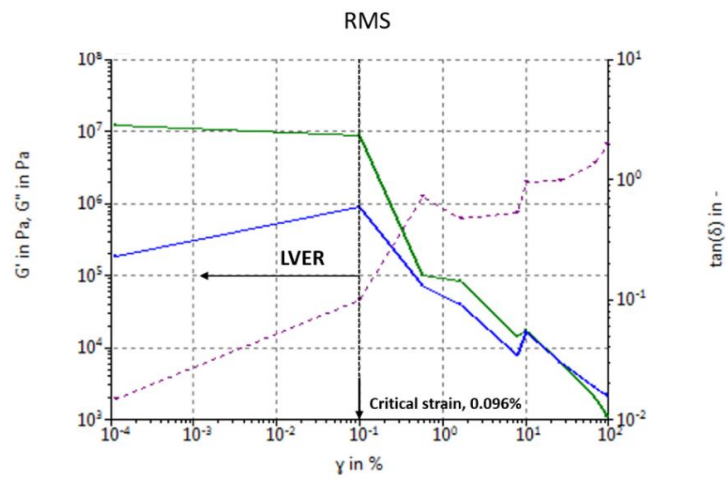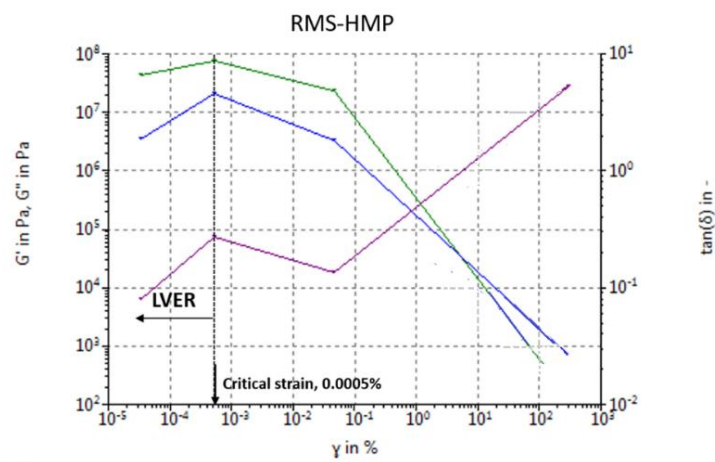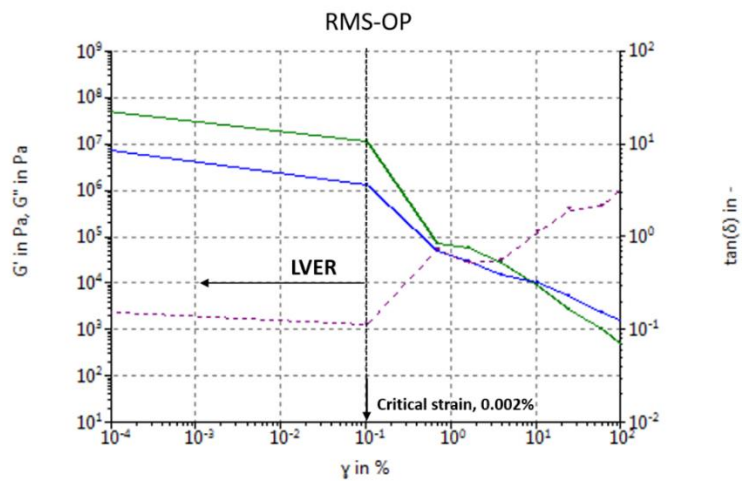532    **Fig. 11** Structural evolution of RMS mixes, showing the (a) storage modulus and (b) phase
533                                                                          angle



(a)



(b)



534
535
536
537
538

539                                                         (c)

540        **Fig. 12** Linear viscoelastic regions (LVER) of (a) RMS, (b) RMS-HMP and (c) RMS-OP mixes

541

542

543    **4. Conclusion**

544

545    This study aimed to develop RMS mixes with suitable properties for potential 3D printing

546    applications. As a part of this goal, the influence of different phosphate additives (HMP, TMP

547    and OP) on the reaction mechanisms and fresh and hardened properties of the developed

548    formulations was evaluated. Out of the 3 superplasticizers used in this study, OP was

549    identified as the most suitable additive for the production of mixes with enhanced hydration

550    and associated performance. The obtained results highlighted that the use of OP in RMS

551    formulations led to higher pH values than other additives, which improved the dissolution of

552    silica and its subsequent reaction with Mg-phases, resulting in the enhanced formation of

553    hydrate phases such as M-S-H. The RMS-OP mix also indicated a consistent workability and

554    better compressive strength that can be translated into a good shape retention, dimensional

555    accuracy and extrudability in 3D printing applications. Understanding the fresh paste

556    reactions kinetics in depth and their influence on fresh and hardened properties can enable

557    the efficient incorporation of additives that can play a major role in improving the printability

558    of alternative binders. Further research on the optimization of mix design, curing conditions

559    and printing parameters can lead to the production of sustainable mixes incorporating novel

560    binders for large scale 3D printed applications.

561

562

563    **Acknowledgements**

564

24

**References:**

[1] C. Sonat, C. Unluer, Investigation of the performance and thermal decomposition of MgO and MgO-SiO$_2$ formulations, Thermochimica Acta 655 (2017) 251-261.

[2] C. Sonat, N. Dung, C. Unluer, Performance and microstructural development of MgO–SiO$_2$ binders under different curing conditions, Construction and Building Materials 154 (2017) 945-955.

[3] C. Sonat, C. Lim, M. Liska, C. Unluer, Recycling and reuse of reactive MgO cements–A feasibility study, Construction and Building Materials 157 (2017) 172-181.

[4] N. Dung, C. Unluer, Improving the performance of reactive MgO cement-based concrete mixes, Construction and Building Materials 126 (2016) 747-758.

[5] N. Dung, C. Unluer, Sequestration of CO$_2$ in reactive MgO cement-based mixes with enhanced hydration mechanisms, Construction and Building Materials 143 (2017) 71-82.

[6] C. Sonat, W. Teo, C. Unluer, Performance and microstructure of MgO-SiO2 concrete under different environments, Construction and Building Materials 184 (2018) 549-564.

[7] S. Kumar, C. Sonat, E.-H. Yang, C. Unluer, Performance of reactive magnesia cement formulations containing fly ash and ground granulated blast-furnace slag, Construction and Building Materials 232 (2020) 117275.

[8] T. Zhang, L.J. Vandeperre, C.R. Cheeseman, Formation of magnesium silicate hydrate (MSH) cement pastes using sodium hexametaphosphate, Cement and Concrete Research 65 (2014) 8-14.

[9] B. Lothenbach, D. Nied, E. L'Hôpital, G. Achiedo, A. Dauzères, Magnesium and calcium silicate hydrates, Cement and Concrete Research 77 (2015) 60-68.

[10] E. Bernard, B. Lothenbach, F. Le Goff, I. Pochard, A. Dauzères, Effect of magnesium on calcium silicate hydrate (CSH), Cement and Concrete Research 97 (2017) 61-72.

[11] T. Zhang, L. Vandeperre, C. Cheeseman, Development of Magnesium Silicate Hydrate cement system for nuclear waste encapsulation, NUWCEM, Avignon2011, pp. 582-591.

[12] J. Chen, T. Li, X. Li, K.C. Chou, X. Hou, Some new perspective on the reaction mechanism of MgO–SiO2–H2O system, International Journal of Applied Ceramic Technology 13(6) (2016) 1164-1172.

[13] F. Jin, A. Al-Tabbaa, Thermogravimetric study on the hydration of reactive magnesia and silica mixture at room temperature, Thermochimica acta 566 (2013) 162-168.

[14] T.T. Zhang, Y.N. Du, Y.J. Sun, Z.M. He, Z.L. Wu, Development of magnesium-silicate-hydrate cement by pulverized fuel ash, Key Engineering Materials, Trans Tech Publ, (2016), pp. 61-65.

[15] P. Pereira, L. Evangelista, J. De Brito, The effect of superplasticisers on the workability and compressive strength of concrete made with fine recycled concrete aggregates, Construction and Building Materials 28(1) (2012) 722-729.

[16] L. Grierson, J. Knight, R. Maharaj, The role of calcium ions and lignosulphonate plasticiser in the hydration of cement, Cement and Concrete Research 35(4) (2005) 631-636.

[17] G.S. Bobrowski, J.D. Connolly, Additive for air-entrained super plasticized concrete, concrete produced thereby and method of producing air-entrained super plasticized concrete, Google Patents, (1982).

[18] R. Combrinck, M. Kayondo, B. le Roux, W. de Villiers, W. Boshoff, Effect of various liquid admixtures on cracking of plastic concrete, Construction and Building Materials 202 (2019) 139-153.

[19] T. Gonçalves, R. Silva, J. de Brito, J. Fernández, A. Esquinas, Mechanical and durability performance of mortars with fine recycled concrete aggregates and reactive magnesium oxide as partial cement replacement, Cement and Concrete Composites (2019) 103420.

[20] Y. Jia, B. Wang, Z. Wu, J. Han, T. Zhang, L.J. Vandeperre, C.R. Cheeseman, Role of sodium hexametaphosphate in MgO/SiO2 cement pastes, Cement and Concrete Research 89 (2016) 63-71.

[21] J. Kruger, S. Cho, S. Zeranka, C. Viljoen, G. van Zijl, 3D concrete printer parameter optimisation for high rate digital construction avoiding plastic collapse, Composites Part B: Engineering 183 (2020) 107660.

[22] M. Sakin, Y.C. Kiroglu, 3D Printing of Buildings: Construction of the Sustainable Houses of the Future by BIM, Energy Procedia 134 (2017) 702-711.

[23] J. Kruger, S. Zeranka, G. van Zijl, A rheology-based quasi-static shape retention model for digitally fabricated concrete, Construction and Building Materials 254 (2020) 119241.

[24] N. Roussel, G. Ovarlez, S. Garrault, C. Brumaud, The origins of thixotropy of fresh cement pastes, Cement and Concrete Research 42(1) (2012) 148-157.

[25] N. Roussel, Rheological requirements for printable concretes, Cement and Concrete Research 112 (2018) 76-85.

[26] B. Panda, G.B. Singh, C. Unluer, M.J. Tan, Synthesis and characterization of one-part geopolymers for extrusion based 3D concrete printing, Journal of Cleaner Production 220 (2019) 610-619.

[27] S.H. Bong, B. Nematollahi, A. Nazari, M. Xia, J. Sanjayan, Method of Optimisation for Ambient Temperature Cured Sustainable Geopolymers for 3D Printing Construction Applications, Materials 12(6) (2019) 902.

[28] J. Kruger, S. Zeranka, G. van Zijl, An ab initio approach for thixotropy characterisation of (nanoparticle-infused) 3D printable concrete, Construction and Building Materials 224 (2019) 372-386.

[29] S. Muthukrishnan, H.W. Kua, L.N. Yu, J.K. Chung, Fresh Properties of Cementitious Materials Containing Rice Husk Ash for Construction 3D Printing, Journal of Materials in Civil Engineering 32(8) (2020) 04020195.

[30] S.H. Bong, B. Nematollahi, M. Xia, A. Nazari, J. Sanjayan, J. Pan, Properties of 3D-Printable Ductile Fibre-Reinforced Geopolymer Composite for Digital Construction Applications, Rheology and Processing of Construction Materials, Springer (2019), pp. 363-372.

[31] J. Sanjayan, J. Pan, Properties of 3D-Printable Ductile Fibre-Reinforced Geopolymer Composite for Digital Construction Applications, Rheology and Processing of Construction Materials: RheoCon2 & SCC9   363.

[32] A. Khalil, X. Wang, K. Celik, 3D printable magnesium oxide concrete: towards sustainable modern architecture, Additive Manufacturing  (2020) 101145.

[33] R. Hay, K. Celik, Hydration, carbonation, strength development and corrosion resistance of reactive MgO cement-based composites, Cement and Concrete Research 128 (2020) 105941.

[34] S.H. Cem Sonat, Junxia Li, Cise Unluer, En-Hua Yang, Strain hardening magnesium-silicate-hydrate composites (SHMSHC) reinforced with short and randomly oriented polyvinyl alcohol microfibers, Cement and Concrete Composites (Under Review) (2020).

[35] G. Mármol, H. Savastano Jr, M.M. Tashima, J.L. Provis, Optimization of the MgOSiO2 binding system for fiber-cement production with cellulosic reinforcing elements, Materials & Design 105 (2016) 251-261.

[36] ASTM International, Standard practice for mechanical mixing of hydraulic cement pastes and mortars of plastic consistency, ASTM International  (2006) 1-3.

[37] ASTM Standard, C1437-07,", Standard Test Method for Flow of Hydraulic Cement Mortar," ASTM International, West Consohocken, PA  (2007).

[38] ASTM, Standard test method for measurement of heat of hydration of hydraulic cementitious materials using isothermal conduction calorimetry,  (2009).

[39] ASTM Testing, M.C.C. Cement, Standard Test Method for Compressive Strength of Hydraulic Cement Mortars (using 2-in. Or [50-mm] Cube Specimens), ASTM International2013.

[40] E. Bernard, B. Lothenbach, D. Rentsch, I. Pochard, A. Dauzères, Formation of magnesium silicate hydrates (MSH), Physics and Chemistry of the Earth, Parts A/B/C 99 (2017) 142-157.

[41] K. Scrivener, R. Snellings, B. Lothenbach, A practical guide to microstructural analysis of cementitious materials, Crc Press (2016).

[42] K.C. Reddy, K.V. Subramaniam, Quantitative phase analysis of slag hydrating in an alkaline environment, Journal of Applied Crystallography 53(2) (2020).

[43] D. Jiao, K. El Cheikh, C. Shi, K. Lesage, G. De Schutter, Structural build-up of cementitious paste with nano-Fe3O4 under time-varying magnetic fields, Cement and Concrete Research 124 (2019) 105857.

[44] I. Navarrete, Y. Kurama, N. Escalona, M. Lopez, Impact of physical and physicochemical properties of supplementary cementitious materials on structural build-up of cement-based pastes, Cement and Concrete Research 130 (2020) 105994.

[45] M. Ramadan, M. Amin, M.A. Sayed, Superior physico-mechanical, fire resistivity, morphological characteristics and gamma radiation shielding of hardened OPC pastes incorporating $ZnFe_2O_4$ spinel nanoparticles, Construction and Building Materials 234 (2020) 117807.

[46] M. Tonelli, F. Martini, A. Milanesi, L. Calucci, M. Geppi, S. Borsacchi, F. Ridi, Effect of phosphate additives on the hydration process of magnesium silicate cements, Journal of Thermal Analysis and Calorimetry 138 (5) (2019) 3311-3321.

[47] P. Bénard, S. Garrault, A. Nonat, C. Cau-Dit-Coumes, Hydration process and rheological properties of cement pastes modified by orthophosphate addition, Journal of the European Ceramic Society 25(11) (2005) 1877-1883.

[48] M. Papachristoforou, V. Mitsopoulos, M. Stefanidou, Evaluation of workability parameters in 3D printing concrete, Procedia Structural Integrity 10 (2018) 155-162.

[49] M. Xia, B. Nematollahi, J. Sanjayan, Printability, accuracy and strength of geopolymer made using powder-based 3D printing for construction applications, Automation in Construction 101 (2019) 179-189.

[50] B. Szostak, G.L. Golewski, Modification of early strength parameters of concrete by the addition of fly ash and admixture of nano CSH for application in 3D printing, MATEC Web of Conferences, EDP Sciences, (2020), p. 01016.

[51] B. Szostak, G.L. Golewski, Improvement of strength parameters of cement matrix with the addition of siliceous fly ash by using nanometric CSH seeds, Energies 13(24) (2020) 6734.

[52] M. Catauro, F. Bollino, F. Papale, M. Gallicchio, S. Pacifico, Synthesis and chemical characterization of new silica polyethylene glycol hybrid nanocomposite materials for controlled drug delivery, Journal of Drug Delivery Science and Technology 24(4) (2014) 320-325.

[53] J. Nordström, E. Nilsson, P. Jarvol, M. Nayeri, A. Palmqvist, J. Bergenholtz, A. Matic, Concentration-and pH-dependence of highly alkaline sodium silicate solutions, Journal of Colloid and Interface Science 356(1) (2011) 37-45.

[54] D. Dimas, I. Giannopoulou, D. Panias, Polymerization in sodium silicate solutions: a fundamental process in geopolymerization technology, Journal of Materials Science 44(14) (2009) 3719-3730.

[55] X. Yang, W. Zhu, Q. Yang, The viscosity properties of sodium silicate solutions, Journal of Solution Chemistry 37(1) (2008) 73-83.

[56] M.E. Simonsen, C. Sønderby, Z. Li, E.G. Søgaard, XPS and FT-IR investigation of silicate polymers, Journal of Materials Science 44(8) (2009) 2079-2088.

[57] C. Roosz, S. Grangeon, P. Blanc, V. Montouillout, B. Lothenbach, P. Henocq, E. Giffaut, P. Vieillard, S. Gaboreau, Crystal structure of magnesium silicate hydrates (MSH): The relation with 2: 1 Mg–Si phyllosilicates, Cement and Concrete Research 73 (2015) 228-237.

[58] S.A. Walling, S.A. Bernal, L.J. Gardner, H. Kinoshita, J.L. Provis, Blast furnace slag-Mg (OH) 2 cements activated by sodium carbonate, RSC Advances 8(41) (2018) 23101-23118.

[59] D. Brew, F. Glasser, Synthesis and characterisation of magnesium silicate hydrate gels, Cement and Concrete Research 35(1) (2005) 85-98.

[60] Y. Zhang, Y. Li, Y. Xu, S. Sang, S. Jin, Enhanced formation of magnesium silica hydrates (MSH) using sodium metasilicate and caustic magnesia in magnesia castables, Ceramics International 43(12) (2017) 9110-9116.

[61] D. Nied, K. Enemark-Rasmussen, E. L'Hopital, J. Skibsted, B. Lothenbach, Properties of magnesium silicate hydrates (MSH), Cement and Concrete Research 79 (2016) 323-332.

[62] N. Roussel, Understanding the rheology of concrete, Elsevier (2011.

[63] Q. Yuan, D. Zhou, K.H. Khayat, D. Feys, C. Shi, On the measurement of evolution of structural build-up of cement paste with time by static yield stress test vs. small amplitude oscillatory shear test, Cement and Concrete Research 99 (2017) 183-189.

[64] M.A. Moeini, M. Hosseinpoor, A. Yahia, Effectiveness of the rheometric methods to evaluate the build-up of cementitious mortars used for 3D printing, Construction and Building Materials 257 (2020) 119551.

**List of Tables:**

**Table 1** Chemical composition (%) of RMC and MS.

|         | RMC  | MS   |
|---------|------|------|
| MgO     | 91.5 | 0.9  |
| $SiO_2$ | 2    | >90  |
| CaO     | 1.6  | -    |
| $R_2O_3$| 1    | -    |
| LOI     | -    | <3   |

**Table 2** FTIR peak assignments for RMS, RMS-HMP and RMS-OP samples.

| Sample | Wavenumber (cm$^{-1}$) | Assignment | Reference |
|---|---|---|---|
| RMS | 1050-1070 | Q$^3$, Si-0-Si (non-bridging oxygen) internal stretching vibrations | [56] |
| | 1100-1200 | Q$^4$ asymmetrical Si-O-Si, external stretching vibrations | [56] |
| RMS-HMP | 1050 | Q$^3$ Si-0-Si (non-bridging oxygen) internal stretching vibrations | [56] |
| | 1110 | Q$^3$ silica vibration in M-S-H | [10] |
| | 1100-1200 | Q$^4$ asymmetrical Si-O-Si, external stretching vibrations | [56] |
| RMS-OP | 990 | Q$^3$ silica vibration in M-S-H | [10] |
| | 1110 | Q$^3$ silica vibration in M-S-H | [10] |
| | 1100-1200 | Q$^4$ asymmetrical Si-O-Si, external stretching vibrations | [56] |

**Table 3** Chemical shifts (ppm) and relative intensities (%) of different Si sites obtained from the deconvolution of the $^{29}$Si MAS NMR spectra.

| Sample (age) | Chemical shift, ppm (relative peak intensities, %) | | | | | | Total unreacted silica (%) |
|---|---|---|---|---|---|---|---|
| | M-S-H | | | | MS | | |
| | $Q^1$ | $Q^2$ | $Q^3$(a) | $Q^3$(b) | $Q^3$ | $Q^4$ | |
| RMS-HMP (1d) | - | -85.5 (2.16) | -91.5 (2.55) | - | -100.9 (12.8) | -111.4 (82.5) | 95.3 |
| RMS-HMP (3d) | -79.8 (7.0) | -85.4 (12.4) | -91.6 (8.3) | -96.7 (0.8) | -100.9 (12.8) | -111.6 (60.1) | 71.5 |
| RMS-OP (1d) | -79.8 (2.9) | -85.5 (9.9) | -91.9 (12.2) | -96.5 (1.1) | -100.9 (15.6) | -111.5 (58.2) | 73.8 |
| RMS-OP (3d) | -79.8 (10.3) | -85.4 (23.3) | -91.9 (25.8) | -96.7 (0.8) | -100.9 (8.8) | -111.8 (30.9) | 39.7 |

**Table 4** Quantification of phases within RMS-HMP and RMS-OP mixes, obtained by XRD analysis.

| Phase | RMS-HMP (1d) | RMS-OP (1d) | RMS-HMP (3d) | RMS-OP (3d) |
|---|---|---|---|---|
| Periclase | 55.9 | 55.6 | 53.4 | 50.3 |
| Brucite | 7.9 | 6.5 | 5.2 | 3.5 |
| Magnesite | 1.1 | 3.2 | 2.8 | 3.1 |
| AmS | 33.0 | 28.5 | 28.2 | 24.5 |
| MSH | 2.1 | 6.2 | 10.4 | 18.6 |